CEAS Aeronaut J
DOI 10.1007/s13272-013-0094-8

ORIGINAL PAPER

# Enhancement of aircraft wake vortex decay in ground proximity

## Experiment versus Simulation

**Anton Stephan · Frank Holzäpfel · Takashi Misaka · Reinhard Geisler · Robert Konrath**

Received: 22 May 2013 / Revised: 7 November 2013 / Accepted: 7 November 2013
© Deutsches Zentrum für Luft- und Raumfahrt e.V. 2013

**Abstract** Aircraft wake vortex evolution in ground proximity is investigated experimentally in a water towing tank, as well as numerically with wall-resolved large eddy simulation (LES). With these complementary instruments the enhancement of wake vortex decay by obstacles, introduced at the ground surface, is analyzed. The experimental methods include time-resolved stereo particle image velocimetry and vortex core visualization. For comparison with the experiment, the LES considers the turbulent wake of the strut, holding the towed aircraft model. Wake vortex trajectories and circulation decay are compared at different distances from the obstacle. Tracers are employed to visualize the obstacle's effects on the vortex core, in LES and experiment. The experimentally obtained trajectories and decay characteristics are reproduced qualitatively by simulations, whereas the agreement is degraded at later times. Beyond that, the vortex dynamics, deduced from the LES results, help to understand the experimental observations. The obstacles trigger helical secondary vortex structures, propagating along the primary vortices. The observed propagation speed of the helical disturbance is fairly well predicted by the suggested simple model. It is shown that the obstacles significantly modify the vortex interaction with the ground and substantially accelerate vortex decay. Two neighboring obstacles lead to colliding disturbances that further enhance vortex decay rates.

**Keywords** Wake vortex flow · Ground effect · Decay enhancement · Large eddy simulation · Towing tank · Particle image velocimetry · Obstacles

A. Stephan (✉) · F. Holzäpfel · T. Misaka
Institut für Physik der Atmosphäre, Deutsches Zentrum für Luft- und Raumfahrt (DLR), 82234 Oberpfaffenhofen, Germany
e-mail: anton.stephan@dlr.de

R. Geisler · R. Konrath
Institut für Aerodynamik und Strömungstechnik, Deutsches Zentrum für Luft- und Raumfahrt (DLR), 37073 Göttingen, Germany

### List of symbols

**Symbols**

| | |
|---|---|
| $\Gamma$ | Circulation, $m^2/s$ |
| $\Gamma_0$ | Initial vortex circulation, $m^2/s$ |
| $\nu$ | Molecular viscosity, $m^2/s$ |
| $\nu_t$ | Turbulent viscosity, $m^2/s$ |
| $\omega$ | Vorticity, 1/s |
| $\omega_x$, $\omega_y$, $\omega_z$ | Vorticity components, 1/s |
| $\rho$ | Density, $kg/m^3$ |
| $\sigma$ | Standard deviation |
| $a$ | Radius of secondary vortex structure, m |
| $A$, $B$ | Parameters for strut wake turbulence model |
| $b_0$ | Initial vortex separation, m |
| $C$ | Chord length, mm |
| $C_D$ | Drag coefficient, 1/m |
| $d$ | Chord thickness, mm |
| $E_{strut}$ | Turbulent kinetic energy of strut wake, Nm |
| $E_\Gamma$ | Turbulent kinetic energy of the vortex, Nm |
| $h_0$ | Initial vortex height, m |
| $L_x$, $L_y$, $L_z$ | Dimensions, m |
| $l_{strut}$ | Length of the strut, m |
| $N_x$, $N_y$, $N_z$ | Grid points |
| $p$ | Pressure, $N/m^2$ |
| $R$ | Curvature radius, m |
| $Re_\Gamma$ | Vortex Reynolds number |
| $Re_c$ | Chord Reynolds number based on towing speed |

Published online: 27 November 2013

| | |
|---|---|
| $r_c$ | Vortex core radius, m |
| $t$ | Time, s |
| $t_0$ | Time unit, s |
| $U_0$ | Towing speed, m/s |
| $u_i$, $u$, $v$, $w$ | Velocity components, m/s |
| $U_{hel}$ | Propagation speed of helix front, m/s |
| $V_0$ | Initial vortex descent speed, m/s |
| $x_i$, $x$, $y$, $z$ | Coordinates, m |
| $\Delta x$ | Distance to obstacle, m |

**Subscripts**

| | |
|---|---|
| 0 | Reference state |
| max | Maximum value |
| rms | Root mean square |
| hel | Helix |
| L | LES |
| ring | Ring |
| W | WSG |

**Superscripts**

| | |
|---|---|
| $'$ | Deviation from reference state |
| * | Normalized with respect to vortex flow |
| + | Normalized by chord length |

**Abbreviations**

| | |
|---|---|
| DLR | German Aerospace Center |
| ICAO | International Civil Aviation Organization |
| LES | Large-eddy simulation |
| PIV | Particle image velocimetry |
| SVS | Secondary vortex structure |
| WSG | Wasser Schleppkanal Göttingen |
| WVAS | Wake vortex advisory system |

## 1 Introduction

As a consequence of lift generation by aircraft wings of limited span, vortex sheets shed off the wings, roll up, and form a pair of counter-rotating vortices. The evolving two-vortex system persists for a long period of time, possessing a high amount of kinetic energy, and thereby, posing a potential hazard to following aircraft. To avoid wake vortex encounters, regulatory separation distances between aircraft weight classes have to be met, which limit the possible handling capacity of an airport. Therefore, the investigation of wake vortex decay is an important issue for commercial aviation [1–3].

The probability to encounter wake vortices increases during the final approach of an aircraft, in the vicinity of the ground. The rebounding vortices may not leave the flight corridor vertically. Due to low height of the aircraft above the ground, the pilot's capabilities to counteract the imposed rolling moment are restricted [4, 5]. This is why the evolution of wake vortices close to the ground has received much attention during the past decade [5–7].

The evolution of a wake vortex system in ground proximity results in a complex three-dimensional flow. Researches show that wake vortex trajectories and decay depend on a variety of parameters. When counter-rotating vortices approach the ground, or are generated at low altitudes, the proximity of a flat surface causes a divergence of the vortices. Induced by the vortices, an outboard directed flow establishes at the ground surface. Vorticity of opposite sign is produced in a boundary layer [8]. The induced flow near the surface experiences an adverse pressure gradient when passing the vortex cores, which is strong enough to cause flow separation, leading to the formation of a separation bubble at the ground. Flow simulations show how pairs of secondary vortices, produced from the separation region, detach and interact with the primary vortices [9–11]. The interaction of the primary and secondary vortices is intensified by environmental turbulence [12]. There have been numerous attempts to accelerate the wake vortex decay by measures at the aircraft. In projects, founded by the European Commission, such as C-Wake, FAR-Wake, and AWIATOR, methods have been presented that modify the wing loading to trigger inherent vortex instabilities [13, 14]. Passive and active devices [15] can be distinguished. However, to the authors' knowledge no work has been done for wake vortex decay acceleration in particular in ground proximity.

In this paper we present a different concept to manipulate vortex decay, based on fundamental properties of vortex dynamics, from two different points of view. With towing tank experiments and large eddy simulations (LES) we investigate the effect of dedicated obstacles placed at the ground, to gain complementary insights into the complex three-dimensional flow fields. Both methods agree qualitatively and reveal that the vortex decay is initiated locally and accelerated globally. To put it simple, the obstacle causes the flow to redirect the force that causes the wake vortices above the obstacle to rebound into accelerated turbulent vortex decay. We further determine quantitatively how much wake vortex decay can be accelerated and compare the results from experiments with LES. In experiments as well as in LES we see that the obstacles trigger disturbances traveling along the primary vortices. We investigate those disturbances for one obstacle as well as their interaction in the case of several obstacles. A thorough analysis of the vortex dynamics can be found in Ref. [12].

The interaction of a counter-rotating two-vortex system with a flat surface, using wall-resolved numerical simulations, has been investigated so far with different approaches. Either wall-resolved direct numerical simulations (DNS) [16] or LES have been employed [17]. The resolution requirements for the boundary layer flow limit the Reynolds number not only in DNS but also in LES. So far,

vortex circulation-based Reynolds numbers around 20,000 have been realized. Similar as in Ref. [17] we conduct wall-resolved LES at a Reynolds number of $Re_\Gamma = 23,130$. The effect of further increased Reynolds numbers is discussed in Ref. [12]. Towing tank experiments are widely used for the investigation of spatially evolving wakes. Turbulent vortex decay is investigated in [18]. The ground effect has been studied in [19, 20]. The experiments are performed in a water tank towing employing a small generic wing model to produce a two-vortex system. Ground plates from transparent PMMA (acrylic glass) introduce flat ground or ground with obstacles. Particle image velocimetry (PIV) recordings measure the velocity vector fields of the wake vortices in certain planes, perpendicular to the towing direction. Black ink is released from the wing tips to visualize the vortex cores.

From the experiments as well as LES we conclude that ground irregularities like obstacles introduce disturbances that are able to destabilize the vortices and to promote their decay. This new method requires relatively small technical effort to be tested and to be introduced at airports, as it is ground based and passive. The effect of a plate line, a further optimization of the obstacles, can be found in Ref. [12]. The corresponding wake vortex decay features may increase safety and potential capacity gains of wake vortex advisory systems (WVAS). The combination of LES and towing tank experiments provides an assessment of the numerical methods. However, this approach is particularly limited by the Reynolds number. The applicability of the described effects in reality has to be investigated with field experiments.

In Sects. 2 and 3 we describe our experimental and numerical setup. In Sect. 4 we present the flow field evolution, in Sect. 5 the analysis of vortex core trajectories and decay. In Sect. 6 we investigate the propagation of end effects, whereas the effects of several obstacles, leading to an interaction of end effects, is studied in Sect. 7. In Sect. 8 we draw the conclusion that the described method effectively accelerates wake vortex decay.

## 2 Experimental setup

### 2.1 Water towing tank and aircraft model

The experiments have been conducted in the DLR water towing tank in Göttingen, termed Wasser Schleppkanal Göttingen (WSG). This facility consists of an 18 m long tank with a cross section of 1.1 m × 1.1 m, equipped with a carriage, capable of crossing the tank at a maximum speed of 5 m/s. Models under investigation can be attached to this carriage and are propelled along the tank at defined velocities, while the water inside the tank is at rest. Compared to a recirculating water tunnel, this approach permits measurements far behind the aircraft model, i.e. old vortex ages. In order to achieve low turbulence levels, the water in the tank was left to rest for at least 20 min prior to each run.

To minimize the influence of the towing tank side walls, a minimum distance of one model span between walls and vortices is required. To ensure this limit, a small version of the DLR F13 aircraft model was build, see Fig. 1b. This model has a rectangular wing with a span of 175 mm and a chord length of 35 mm. The profile is a Wortman FX63-137B-PT. Embedded in the wing tips are outlets for contrast agents to trace the vortex cores. The model is supported by a profiled strut, attached to the carriage via a translation stage. By this means, the vertical position of the model can be adjusted. For the present experiments, the angle-of-attack is set to 10° and the tail wing is replaced by a cone tail. The initial measured vortex separation is $b_0 = 153$ mm, the model is towed with 2.44 m/s through the tank, which leads to an initial measured circulation of $\Gamma_0 = 0.052\,\mathrm{m}^2/\mathrm{s}$, an initial measured descent speed of $V_0 = 49\,\mathrm{mm/s}$, and a resulting reference time $t_0 = b_0/V_0 = 3.1\,\mathrm{s}$. The corresponding Reynolds number is $Re_\Gamma = \Gamma_0/\nu = 52,000$, with $\nu = \nu_{\mathrm{water}} = 10^{-6}\,\mathrm{m}^2/\mathrm{s}$. These values are used for normalization in the experimental setup. Flat ground, one bar-shaped obstacle as well as two obstacles with a separation of $\Delta x/b_0 = 7.2$ have been investigated.

### 2.2 Stereo PIV

The velocity vector fields ($u$, $v$, $w$) of the wake vortices are measured in a certain plane, by means of a time-resolved stereo particle image velocimetry (PIV) system. Polyamide particles of 20 µm average diameter and $1.03\,\mathrm{g/cm}^3$ density are suspended into the water as tracer particles. They are illuminated by a Lee LDP 200-MQG laser at 1 kHz repetition rate with a pulse energy of 25 mJ. The laser beam is expanded and refocused by a telescope, and finally spread out to a light sheet by a cylindrical lens. This light sheet is brought into the towing tank from the side with a final orientation perpendicular to the towing direction. Two Photron APX-RS high-speed cameras record the light, scattered by the polyamide particles from both sides of the light sheet. To reduce aberrations, glass prisms, filled with water, are attached to the sides of the tank with their air–glass interfaces perpendicular to the respective camera line of vision. Scheimpflug correction is applied to ensure image sharpness for the complete field of view.

The imaging system is calibrated by taking photos of a calibration grid, printed on a glass plate in the water at the light sheet position. Laser and cameras are controlled by a

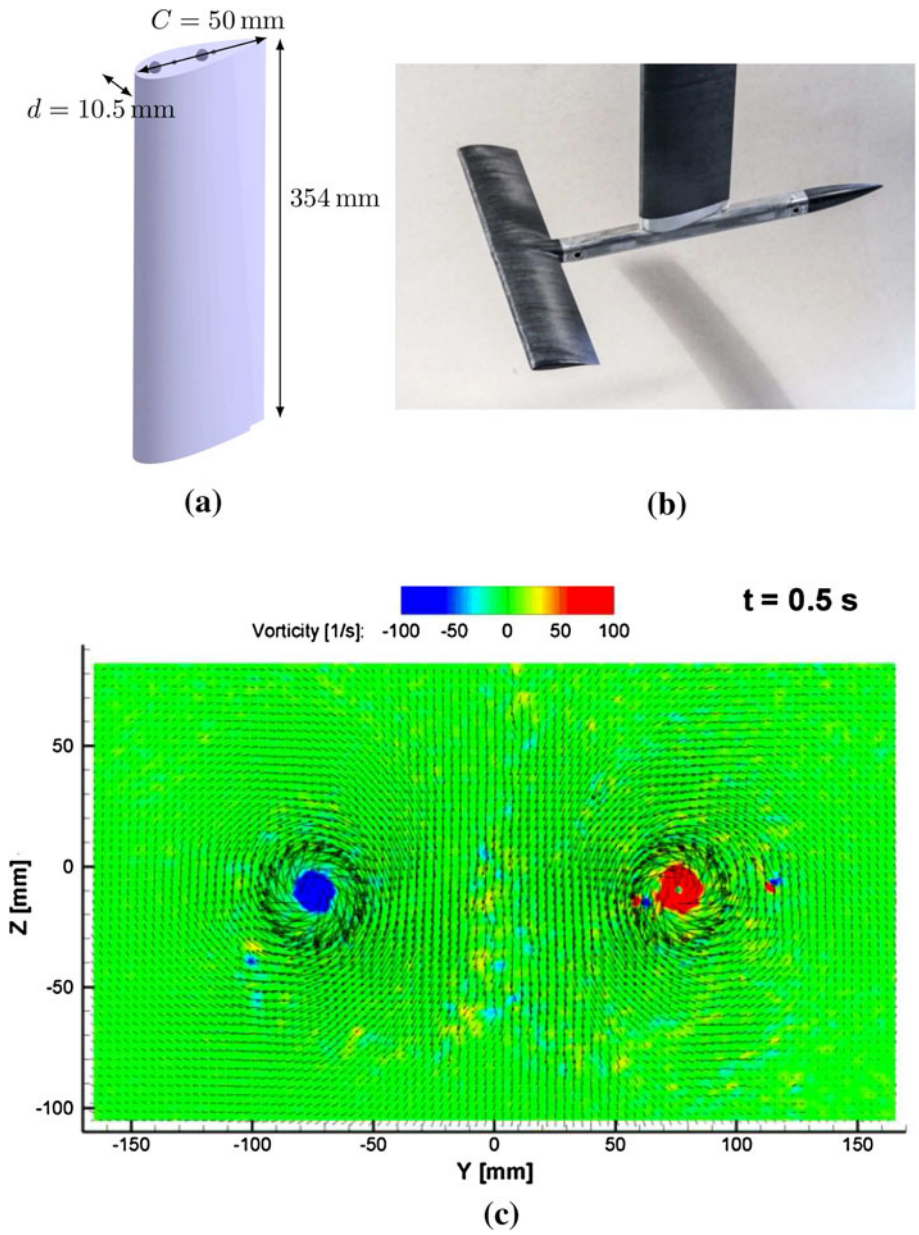


**Fig. 1** **a** Schematic of the strut. **b** Aircraft model. **c** Strut wake turbulence, vorticity (*color coded*), and velocity vectors (*small dashes*) measured at high altitudes above ground by PIV

programmable sequencer, triggered by a magnetic switch from the model carriage.

Wake vortices feature a decreasing dynamic range of velocities. Thus, the delay used for PIV recordings has to be adapted accordingly. In the current application, PIV images are recorded at times of 0, 2, 5, 10, and 20 ms. This sequence is repeated every 50 ms. Using this scheme, the PIV delay can be selected and adapted to the actually occurring velocity range after the recording, while maintaining a sufficient time resolution of 20 vector fields per second, as well as a long total observation time (limited by camera RAM). The acquired images are evaluated using a well-established multi-grid cross-correlation analysis with image deformation. Disparity correction with the final light sheet is applied to compensate for the refraction, caused by the glass calibration grid carrier. Depending on the time separation of recorded images, i.e. $dt$ = 2–20 ms, the uncertainty of the velocity is estimated at 2–20 mm/s that corresponds to about 1–2 % of the maximal velocity in the flow field.

### 2.3 Vortex core visualization

Since PIV provides only local planar information on the wake vortices, vortex core visualization has also been applied. Driven by gravity, black ink from a vessel, 0.5 m above the water surface, is fed into the tube system of the model and finally released into the vortex cores through

outlets at the wing tips. Since in this setup the view from below the tank is spoiled by constructions supporting the transparent ground plate and the obstacles, as well as by bubbles below the ground plate, the ink traces are recorded with background illumination from above the tank by a consumer-grade HD video camcorder. Since calibration and quantitative evaluation here are hindered by the surface waves of the water, only qualitative results can be obtained in this configuration.

### 2.4 Strut wake turbulence

For an appropriate modeling of the experiments with LES, it is not sufficient just to model the rolled-up vortices, as with the relatively low Reynolds number, that we employ in the simulations, the vortex ground interaction would remain laminar for a long time. As an important source of turbulence generated by the towed aircraft model, which is identified by the experimenters, we focus on the wake of the profiled strut, see Fig. 1c. Other sources of turbulence like strut–body junction vortices as well as the turbulence generated during the vortex roll-up are not taken into account. This way we do not account for the turbulent vortex roll up process observed in field measurements, but include a reasonable source of turbulence observed in the experiments. Figure 1a depicts the geometry and dimensions of the symmetric profile. The airfoil (strut) chord length $C$ is 50 mm, maximal thickness of the airfoil $d$ is 10.5 mm. The chord Reynolds number, based on the towing speed, is $Re_c = 1.22 \times 10^5$. The vertical turbulence structures behind the strut are transported downwards and stretched in the primary vortex field, see Fig. 1c. The turbulence structures behind a symmetric airfoil at comparable Reynolds numbers are carefully studied in Refs. [21, 22].

From the results in Ref. [21] we deduce the turbulence characteristics in the wake. From the measured turbulence profiles presented in Ref. [21] we postulate diffusion type similarity profiles for the fluctuation velocity $u_{\mathrm{rms}}$:

$$u_{\mathrm{rms}}(y,t) = \frac{B\nu_t}{\sqrt{4\pi\nu_t t}} \cdot \exp\left(-\frac{1}{2}\left(\frac{y}{\sqrt{2\nu_t t}}\right)^2\right), \tag{1}$$

with $\nu_t$ representing a turbulent viscosity. If we normalize $u_{\mathrm{rms}}$ by the towing speed $U_0$, and axial and lateral coordinates by the chord length $C$, $x^+ = x/C$, $y^+ = y/C$ and assume $x \sim t \cdot U_0$ we get

$$\frac{u_{\mathrm{rms}}}{U_0} = \frac{A \cdot B}{\sqrt{2\pi}\sigma^+(x^+)} \cdot \exp\left(-\frac{1}{2}\left(\frac{y^+}{\sigma^+(x^+)}\right)^2\right), \tag{2}$$

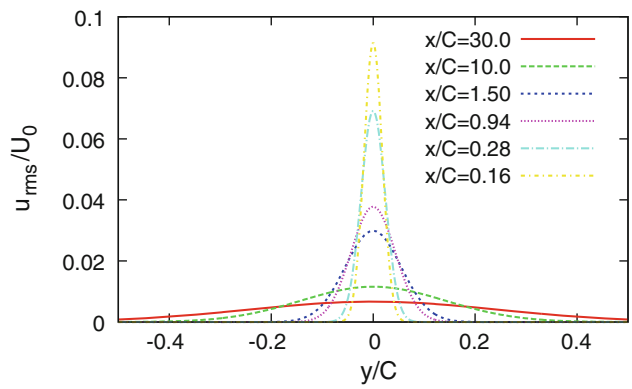


**Fig. 2** Streamwise turbulence intensity distributions for different distances from the strut

where

$$\sigma^+(x^+) = \sqrt{2Ax^+}, \quad A = \frac{\nu_t}{U_0 C}. \tag{3}$$

We fit the data presented in [21] and get $B = 4.1$ and $A = 0.001$. For simplicity we scale

$$v_{\mathrm{rms}}/U_0 = w_{\mathrm{rms}}/U_0 = u_{\mathrm{rms}}/U_0 \tag{4}$$

which holds in the far wake. Figure 2 depicts the resulting similarity profiles.

## 3 Numerical setup

### 3.1 Numerical method

The LES is performed using the incompressible Navier–Stokes code MGLET, developed at Technische Universität München [23], for solving the Navier–Stokes equations and the continuity equation

$$\frac{\partial u_i}{\partial t} + \frac{\partial(u_i u_j)}{\partial x_j} = -\frac{1}{\rho}\frac{\partial p'}{\partial x_i} + \frac{\partial}{\partial x_j}\left((\nu + \nu_t)2S_{ij}\right) \tag{5}$$

$$\frac{\partial u_j}{\partial x_j} = 0. \tag{6}$$

Here $u_i$ represents the velocity components in three spatial directions ($i = 1, 2,$ or $3$), $S_{ij} = (\partial u_i/\partial x_j + \partial u_j/\partial x_i)/2$ denotes the strain rate tensor, and $p' = p - p_0$ equals the deviation from the reference state $p_0$. Molecular viscosity $\nu$ is set to $2.29 \times 10^{-2}\ \mathrm{m^2/s}$ and eddy viscosity $\nu_t$ is obtained by a Lagrangian dynamic subgrid-scale model [24]. A standard Smagorinsky model overestimates the eddy viscosity in the centrifugally stable vortex core, so different correction procedures are employed in literature [25, 26]. The Lagrangian dynamic subgrid scale model overcomes that problem, as the model coefficients are calculated locally and averaged along path-lines. For density $\rho = 1.2\ \mathrm{kg/m^3}$ is

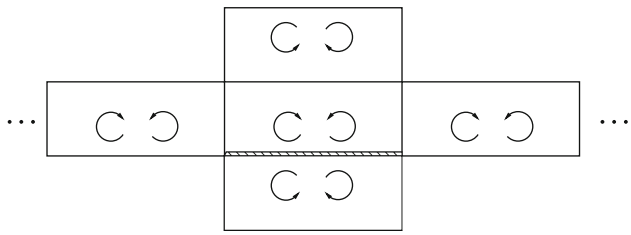

**Fig. 3** Schematic of the wake vortex initialization employing mirror and image vortices

employed. Equations (5) and (6) are solved by a finite-volume approach with a fourth-order finite-volume compact scheme [27]. The simulations are performed in parallel using a domain decomposition approach.

### 3.2 Initial vortex pair

The fully rolled-up wake vortices are initialized by a pair of counter rotating Lamb–Oseen vortices with a circulation of $\Gamma_0 = 530\,\mathrm{m}^2/\mathrm{s}$, a vortex core radius of $r_c = 3.0$ m and a vortex separation $b_0 = 47.1$ m, which are representative values for a heavy aircraft. The Reynolds number is set to $Re_\Gamma = \Gamma_0/\nu = 23,130$. The velocity scale is based on the inviscid initial descent speed of the vortex pair $V_0 = \Gamma_0/2\pi b_0 = 1.79\,\mathrm{m/s}$. This defines the non-dimensional time $t^* = t \cdot V_0/b_0$ with $t_0 = b_0/V_0 = 26.3\,\mathrm{s}$ and vorticity $\omega^* = \omega t_0$. Lengths are non-dimensionalized by $b_0$ and velocities by $V_0$, if marked with an asterisk. For prescribing the initial vortex velocity field, six periodically arranged image vortex pairs in spanwise direction and two mirror vortices in the direction perpendicular to the ground are taken into account, see Fig. 3. This way a smooth transition at periodic boundaries of the initial field is achieved, and vertical velocity components at the top and bottom of the domain are nearly zero, eliminating disturbances at the boundaries after initialization. Note that we face a significant difference to the experiments, where vortices are generated by a wing model towed through a water tank. The vortices still need to roll up when they are generated at a height of $b_0/2$. However, unlike for high-lift wing configurations, vortex sheets shed off uniformly. In clean configuration the roll-up is finalized very fast [28]. Thus we assume that after the roll-up process LES and experiments coincide approximately. Directly above the obstacles the roll-up effect may lead to differences to the LES results, though.

### 3.3 Computational domain

In our simulations we use a computational domain size with dimensions $L_x = 384\,\mathrm{m}, L_y = 288\,\mathrm{m}, L_z = 96\,\mathrm{m}$, see Fig. 4. This corresponds to approximately $8b_0 \times 6b_0 \times 2b_0$. The initial height of the vortex pair is set to $h_0 = b_0/2$.

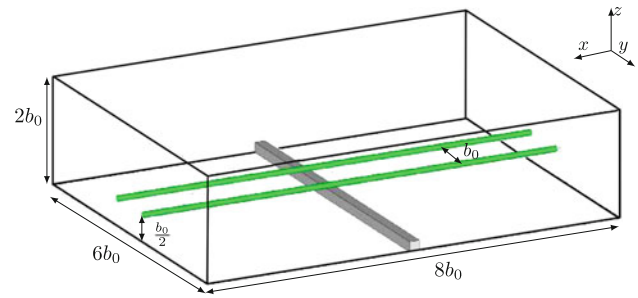


**Fig. 4** Schematic of the computational domain with the initial vortex position and an obstacle

We impose periodic boundary conditions in the $x$ and $y$ directions. A no-slip condition is set at the ground at $z = 0$ and a slip condition at the top at $z = z_{\max}$. The number of grid points are $N_x = 512, N_y = 384, N_z = 192$, leading to a total of 37.7 million grid points. We employ a horizontally equidistant mesh. In vertical direction the mesh is stretched geometrically up to a height of $b_0$ and then continued equidistantly. The interaction of wake vortices with obstacles develops in all three spatial directions. The axially propagating disturbance requires a large extent of the $x$ dimension to exclude boundary effects. The simulations cover the range that was used for the investigation of two obstacles in the experiments. The employed mesh spacing equals three-quarters of the spacing used in [28]. This mesh resolution guarantees that 8 intervals resolve the vortex core and keep it tight in time [12]. Secondary vortices generated at the ground are just vertically well resolved due to mesh stretching. The horizontal resolution of 0.75 m is the same as used in [17].

### 3.4 Obstacles

Obstacles at the ground surface are introduced to trigger the formation of secondary vortex structures (SVS) and to achieve premature vortex decay. We impose obstacles at the ground surface in the center of the domain, perpendicular to flight direction, with a square-shaped cross section of $9\,\mathrm{m} \times 9\,\mathrm{m} \sim 0.2b_0 \times 0.2b_0$, see Fig. 4. For reasons of numerical stability we cannot set the velocity inside the obstacle to zero. Instead, the obstacles are modeled by adding a drag force source term $F_{D,i} = C_\mathrm{D}|u|u_i$ to the Navier–Stokes equations with a large drag coefficient $C_\mathrm{D} = 10/\mathrm{m}$.

### 3.5 Wake turbulence of the strut

We simulate the wake of the strut for the case of a flat ground. For this purpose we generate an isotropic turbulence field, based on the stochastic noise generation approach using the von Karman and Pao spectrum [29] in a

separate simulation. The energy spectrum is initialized using the results from [22]. The LES of decaying turbulence is performed in a $(2b_0)^3$ domain, until the eddy dissipation rate reaches its maximum value in time. At that time, the energy density spectrum, depicted in Fig. 5, has formed a $-5/3$ slope. We weight the initial isotropic turbulence field using the similarity profiles given in Eq. (2). The maximum value of $u_{\mathrm{rms}}$ is scaled from the experiment to LES, assuming that the ratio of the turbulent kinetic energy in the strut wake and in the two wake vortices is constant.

$$\frac{E_{\mathrm{strut}}}{E_\Gamma} = \mathrm{const.} \tag{7}$$

For the kinetic energy per distance of Lamb–Oseen vortices, in the case that $r_c/b_0 < 0.2$, we employ [30]:

$$\frac{E_\Gamma}{\mathrm{d}x} = \frac{\rho \Gamma^2}{2\pi}\{\log(b_0/r_c) + 0.0562\}. \tag{8}$$

Computing the turbulent kinetic energy per distance in the strut wake, we get with Eq. (2)

$$\frac{E_{\mathrm{strut}}}{\mathrm{d}x} = \int_0^{l_{\mathrm{strut}}} \int_{-\infty}^{\infty} \frac{3}{2}\rho u_{\mathrm{rms}}^2 \mathrm{d}y\mathrm{d}z = l_{\mathrm{strut}}\rho\frac{3}{2}u_{\mathrm{rms,max}}^2 \int_{-\infty}^{\infty} \mathrm{e}^{\left(-\frac{1}{2}\left(\frac{y}{\sigma}\right)^2\right)}\mathrm{d}y = \frac{3}{2}\sqrt{2\pi} l_{\mathrm{strut}}\sigma\rho u_{\mathrm{rms,max}}^2. \tag{9}$$

The strut length is scaled with the vortex separation $b_0$. From (7)–(9) we get a relation for the turbulence levels

$$\frac{\sigma_{\mathrm{L}}\rho_{\mathrm{L}} b_{0,\mathrm{L}} u_{\mathrm{rms,max,L}}^2}{\sigma_{\mathrm{W}}\rho_{\mathrm{W}} b_{0,\mathrm{W}} u_{\mathrm{rms,max,W}}^2} = \frac{\rho_{\mathrm{L}}\Gamma_{\mathrm{L}}^2\{\log(b_{0,\mathrm{L}}/r_{\mathrm{c,L}}) + 0.0562\}}{\rho_{\mathrm{W}}\Gamma_{\mathrm{W}}^2\{\log(b_{0,\mathrm{W}}/r_{\mathrm{c,W}}) + 0.0562\}}, \tag{10}$$

in the LES (index L) and WSG (index W).

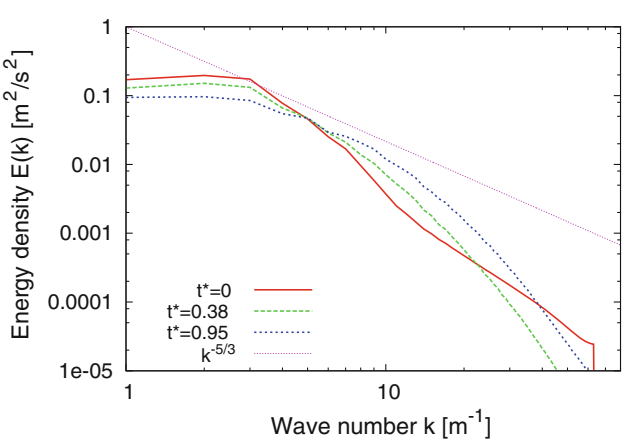


**Fig. 5** Energy density spectra established during separate simulation

For initializing turbulence we assume that the standard deviations of the similarity profiles in Eq. (2) scale with $b_0$.

$$\frac{\sigma_{\mathrm{W}}}{\sigma_{\mathrm{L}}} = \frac{b_{0,\mathrm{W}}}{b_{0,\mathrm{L}}}$$

which yields

$$u_{\mathrm{rms,max,L}} = u_{\mathrm{rms,max,W}}\frac{\Gamma_{\mathrm{L}}/b_{0,\mathrm{L}}}{\Gamma_{\mathrm{W}}/b_{0,\mathrm{W}}}\sqrt{\frac{\log(b_{0,\mathrm{L}}/r_{\mathrm{c,L}}) + 0.0562}{\log(b_{0,\mathrm{W}}/r_{\mathrm{c,W}}) + 0.0562}} \tag{11}$$

Hence, the maximal $u_{\mathrm{rms}}$ values scale approximately according to the vortex descent velocities times a coefficient depending on the vortex characteristics. The above calculated $u_{\mathrm{rms}}$ values and the initial parameters listed in Table 1 yield $u_{\mathrm{rms,\ max,\ L}} = u_{\mathrm{rms,\ max,\ W}}$*35.5. For turbulence initialization in the LES we choose $x^+ = 30$, corresponding to $\sigma_W^+(30) = 0.245$, $\sigma_L = 0.38\ m$ and $u_{\mathrm{rms,\ max,\ L}} = 0.0163$ m/s $\times$ 35.5 = 0.58 m/s.

Finally, the turbulence field is mapped periodically to the simulation domain according to Eq. (2).

## 4 Flow phenomenology

LES allows three-dimensional evaluation of arbitrary quantities derived from the velocity and pressure fields. In the experiments we have to stick to the quantities we can derive from the imaging methods. On the other hand, experiments reflect real fluid dynamics, so LES and towing tank experiments are complementary for analyzing flow phenomena. In order to ensure comparability of the two methods, we use a similar Reynolds number.

### 4.1 Simulation

When the vortex pair descends it induces a vorticity layer at the ground, see Fig. 9 (left) [8]. The vorticity at the ground

**Table 1** Initial parameters in the experimental and numerical set-up

| | $Re_\Gamma$ | $\Gamma_0$ (m²/s) | $b_0$ (m) | $V_0$ (m/s) | ρ (kg/m³) | $r_{c,0}$ (m) |
|---|---|---|---|---|---|---|
| WSG | 52000 | 0.052 | 0.153 | 0.049 | 1000 | 0.09 |
| LES | 23130 | 530 | 47.1 | 1.79 | 1.2 | 3 |

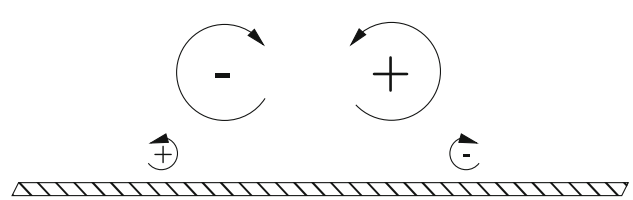


**Fig. 6** Sketch of wake vortex flow

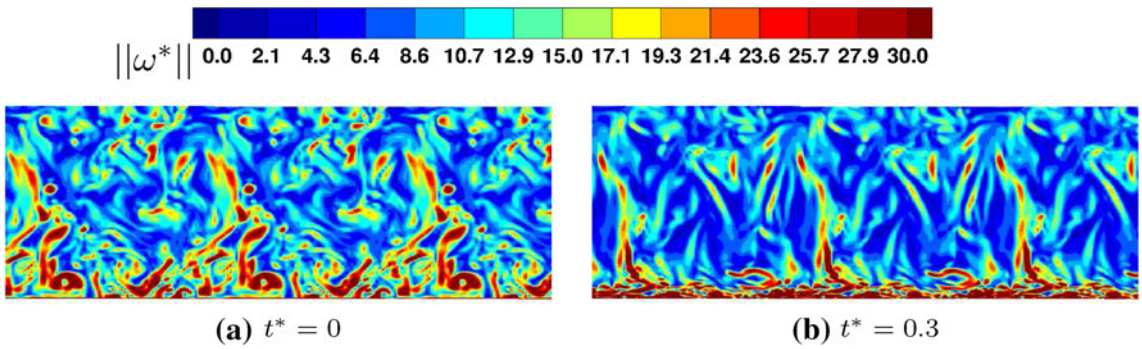


**Fig. 7** Stretching and tilting of wake turbulence between the primary vortices. Center slice colored by vorticity magnitude ||ω*||

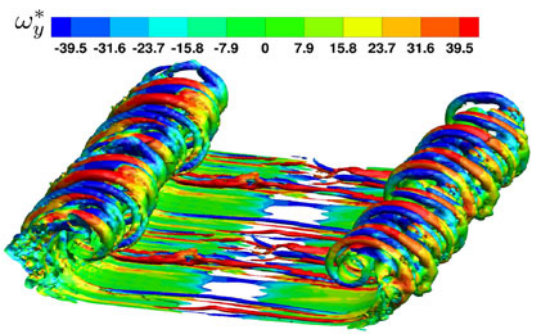


**Fig. 8** Iso-surfaces of $\|w^*\| = 79$ colored by vorticity strength $\omega_y^*$ in spanwise direction at $t^* = 0.91$. Cutout from the original domain. Roll-up of secondary vortex structures generated by strut turbulence

has the opposite sign than the primary vortices, Fig. 6. The magnitudes of the wake-vortex induced vorticity layers are growing, leading eventually to separation and the generation of counter-rotating vortices. Then, the secondary vortices rebound and rotate around the primary vortices.

In contrast to the wake vortex decay mechanisms that appear aloft, and which are driven by atmospheric turbulence and thermal stratification [31, 32], the primary origin of turbulence in the LES is the turbulent strut wake, as modeled in Sect. 2.4, see Fig. 7. The turbulent structures generated by the strut are stretched around the primary vortices and quickly transported to the ground between the vortex pair, disturbing the formation of the secondary vortices. Hence, the secondary vortices are destabilized in their development, generating irregularities. The counter-rotating secondary vortices finally develop into relatively strong turbulent structures initiating rapid vortex decay of the primary vortices. Figure 8 shows how those secondary vorticity structures (SVS) develop from the ground effect vortices. A detailed analysis of the impact of ground turbulence on the SVS can be found in Ref. [12].

The obstacle changes the flow field significantly. At the top of the barrier secondary vorticity is generated rapidly after vortex initialization, which subsequently detaches and develops a distinct loop, see Fig. 9 (right). The loop is stretched and winds around the primary vortex forming an omega shape, approaching and immersing into the primary vortex. The process follows the vortex stretching and tilting mechanisms detailed in Ref. [31]. The geometrically induced SVS travel along the primary vortices, driven by self-induced velocity induction, see Fig. 14,

until they collide at the boundary of the periodic domain. Comparing the evolution of the wake vortex pairs over flat terrain (Fig. 9, left) and over terrain with the obstacle (right), it is obvious that the obstacle triggers significantly more rapid and vigorous decay.

### 4.2 Experiment

Experiments have been conducted with flat ground as well as with obstacles. For comparison with the experimental vortex core visualizations in the LES we initialize a passive tracer concentrated in the core. In the case of a square obstacle (cross section $0.2b_0 \times 0.2b_0$ as in the LES) oriented perpendicular to the towing direction, see Fig. 10 (left), we see disturbances emerging and traveling upstream and downstream from the point where the vortex first hits the obstacle. So the ink is transported in axial directions to both sides. LES show similar behavior, see Fig. 10 (right) and reveal that these disturbances are correlated with the forefront of the wound up secondary vortices. Although in the experiments we cannot see the secondary vortices directly we get an impression of how they act on the primary vortices. Later we will analyze the speed of these disturbances in more detail. Note the bursting of the vortex core during the passage of the disturbance associated with an agglomeration of the tracer marked fluid at the head of the disturbance in both experiment and simulation.

PIV recordings are taken in vertical planes at different distances from the obstacle, $\Delta x^* = 0, \Delta x^* = 1.05$, and $\Delta x^* = 3.6$ and at a single position in case of flat ground. From the gained time-resolved 3-component velocity vector fields we evaluate properties like vorticity and vortex circulation, as well as vortex core traces. In Fig. 11 we see how

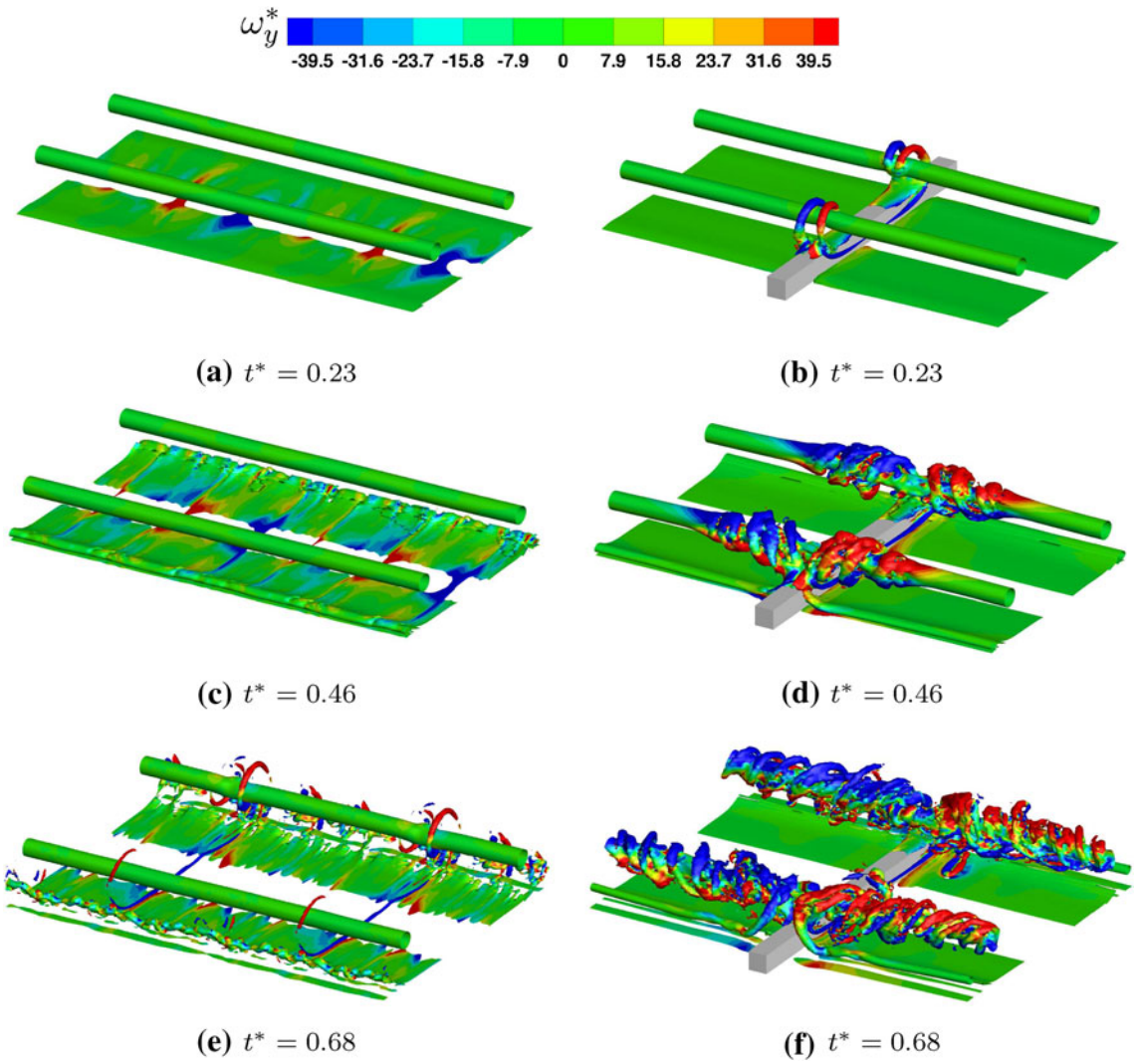


**Fig. 9** Wake vortex evolution without (*left*) and with square-shaped obstacle at the ground (*right*). Iso-surfaces of $\|w^*\| = 79$ colored by vorticity strength $\omega_y^*$ in spanwise direction. Cutout from the original domain

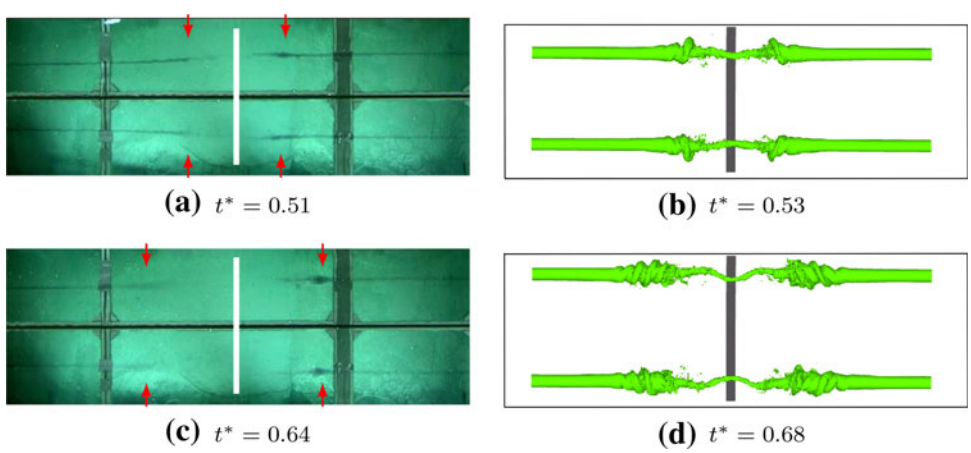


**Fig. 10** Obstacle effects. Vortex cores visualization in towing tank (**a**) and (**c**), LES with passive tracer (**b**) and (**d**). *White bars* show the obstacle position. *Arrows* pointing at disturbance caused by obstacle

a vorticity layer with opposite sign is generated at the ground. We observe that the vortex does not rebound significantly in the region of the obstacle but stays close to it. Already at $t^* = 1.6$ the vortex is much more disturbed above the obstacle than above flat ground. Comparing vorticity distributions and velocity vectors in Fig. 11c and d indicates that at

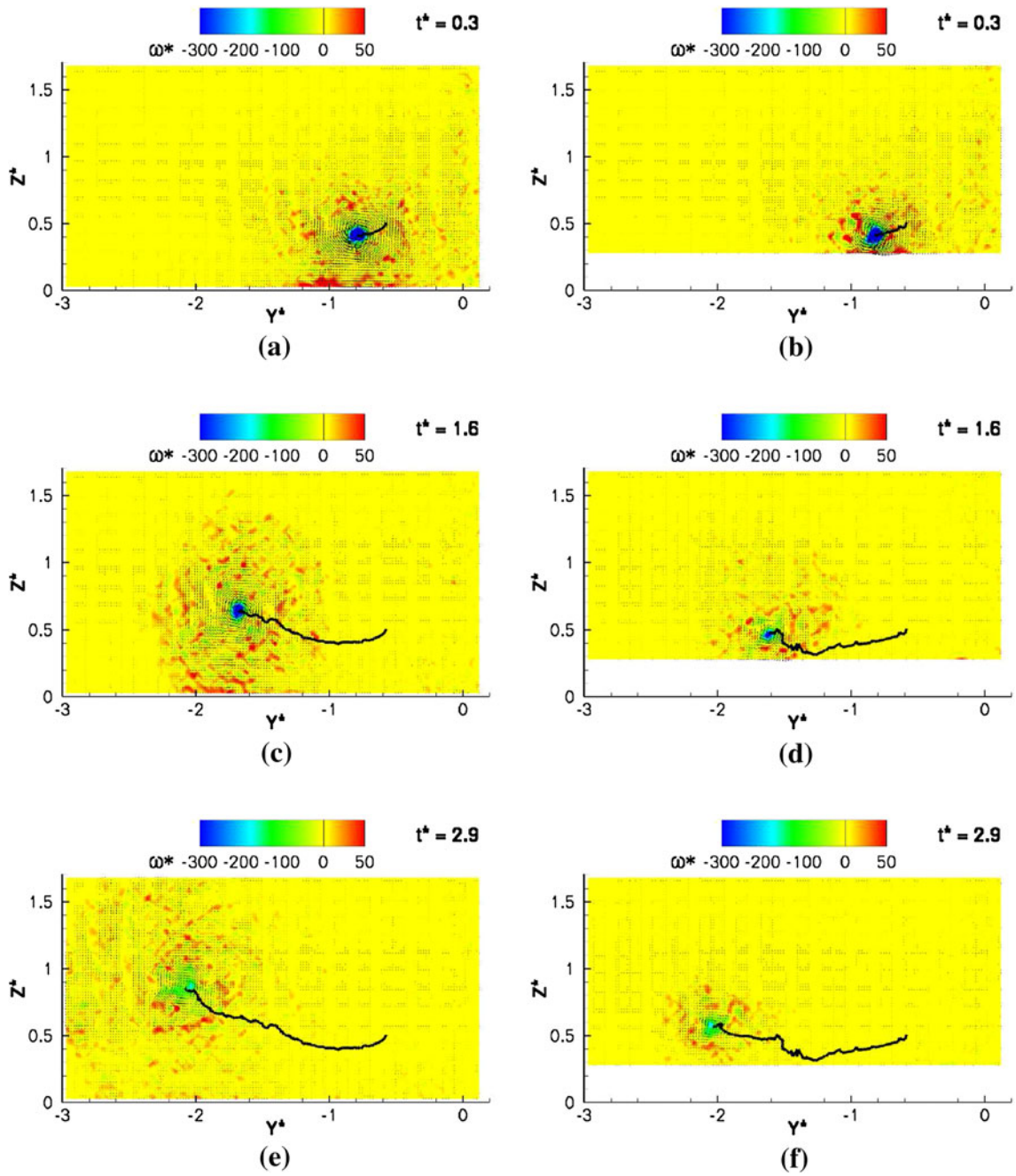


**Fig. 11** Vorticity (*color coded*), velocity vectors (*small dashes*) and vortex tracks (*black lines*) measured by PIV above flat ground (*left*) and above the obstacle (*right*)

$t^* = 1.6$ the vortex at the obstacle has already substantially lost its strength. However, this visual survey cannot replace quantitative evaluation and comparison of trajectories and vortex decay, performed in the next section.

## 5 Trajectories and decay

Knowledge and prediction of the position and the strength of the wake vortices is important for wake vortex advisory systems [33]. The primary vortex centers are tracked detecting local pressure minima and extreme values of vorticity in LES, and local centroids of vorticity distributions in the PIV measurements [34]. Experimental data, depicted in the plots in this paragraph, represent quantities in the observation plane averaged over 3–5 runs. For LES we have to keep in mind that we use periodic boundary conditions. So, interpreting the simulations correctly, we do not calculate the influence of one obstacle, but periodically arranged obstacles with a separation equal to the domain length. However, until

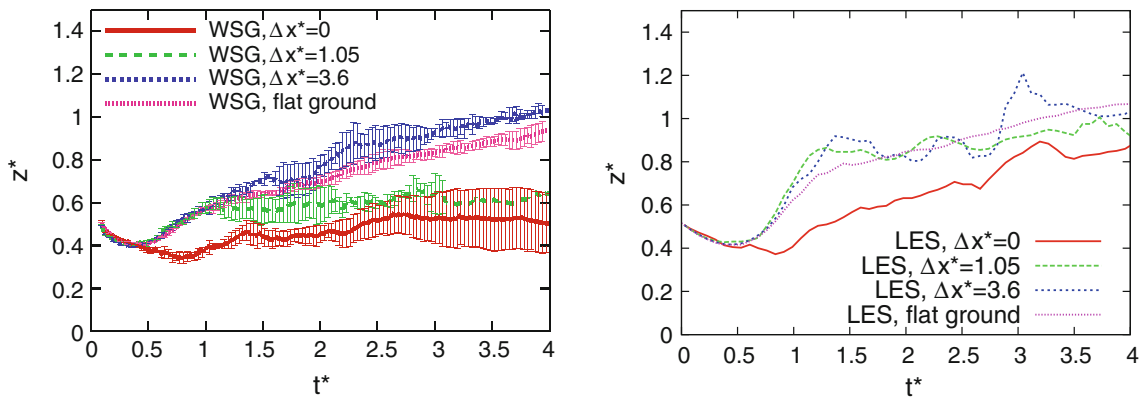


**Fig. 12** Vortex trajectories derived from PIV with standard deviations (*left*) and derived from LES (*right*), at different distances from a $0.2b_0 \times 0.2b_0$ square obstacle and above flat ground

the disturbance reaches the domain boundary in flight direction, which occurs roughly at $t^* = 1$, we can neglect the influence of other obstacles enabling a comparison with experiments. At approximately $t^* = 0.9$ the disturbances start to collide at the periodic boundaries, leading to vortex bursting after $t^* = 1.0$, see Sect. 7. Therefore, we may not expect exactly the same behavior in the experiments with one obstacle and the LES after $t^* = 1.0$.

Figure 12 shows the impact of an obstacle on wake vortex rebound height. For different distances to the obstacle, as well as flat ground, rebound heights are plotted against time. Error bars depict the uncertainties in the experimental results.[1] Initialized at $b_0/2$, the primary vortices descend in the experiments above flat ground to a height of about $0.4b_0$ at $t^* = 0.4$, Fig. 12 left. They rebound and rise with an approximately constant rate of $0.1b_0$ per $t_0$ from $t^* = 1$ to $t^* = 4$. Directly above the obstacle the vortex descent is stronger pronounced, and the rebound height is very much reduced to be $<0.6b_0$ during the entire measurement time. Apart from the obstacle the rebound height coincides with the flat ground case until $t^* = 1$ and develops differently thereafter. The maximal rebound height increases with the distance to the obstacle. We even observe that at a distance of $3.6b_0$ the rebound height exceeds the height above flat ground. Though the difference is small, it is statistically valid, see Fig. 12a. In the LES the interaction of a vortex with flat ground is very similar during the complete computation time. Only between $t^* = 0.7$ and $t^* = 1.5$ the LES show slightly higher rebound altitudes, continuing with nearly the same ascent rate as in the experiments. With an obstacle the rebound characteristics are similar as in the experiments until $t^* = 1$. The trajectories are close in all considered distances. The minimum vortex height of $0.4b_0$ is achieved at around $t^* = 0.5$ in distances $\Delta x^* = 1.05$ and $\Delta x^* = 3.6$. Above the obstacle the vortices descend stronger to a minimum height shortly before $t^* = 1$. However, for $t^* > 1$ we observe distinct differences. Observing still similar rebound behavior in a distance $\Delta x^* = 3.6$ fluctuating around the experimental results we have much higher rebound altitudes closer to the obstacle at $\Delta x^* = 0$ and $\Delta x^* = 1.05$. At $\Delta x^* = 0$ the vortices meander between $0.4b_0$ and $0.5b_0$ in the experiments, whereas they continuously rebound in the LES to a height of almost $0.9b_0$ at $t^* = 4$. Note that the altitudes in the experiments above the obstacle feature the largest scatter. So the deviations between experiments and simulations above the obstacle may partly be attributed to the large variability of the already weakened vortices. At $\Delta x^* = 1.05$ the vortices stay close to a constant level of $0.6b_0$ in the experiments, but vary between 0.8 and $1b_0$ in the LES.

Of major interest is the vortex strength that potentially may affect an aircraft. As a common measure of the vortex strength we investigate the development of the circulation $\Gamma$. Let $\Gamma(r) = \oint \vec{u} \cdot d\vec{s}$ be the circulation along a circle in a $x$-plane with radius $r$, centered in the primary vortex center. In literature $\Gamma_{\max} = \max_r\{\Gamma(r)\}$ is considered as well as $\Gamma_{5-15} = \frac{1}{10}\int_{5\mathrm{m}}^{15\mathrm{m}} \Gamma(r)\mathrm{d}r$, as a common value for circulation of sufficiently large aircraft [35]; however, they allow different interpretations. The averaged quantity $\Gamma_{5-15}$ reflects the mixing with the secondary vortices, with vorticity of opposite sign. $\Gamma_{\max}$ is of physical interest as it reveals the actual maximal strength of a vortex. Both, in the experiments as well as in the simulations, we present just $\Gamma_{\max}$.

Above the obstacle we observe a tremendous reduction of circulation during the first $t_0$, compared with the flat ground case. The experiment shows a reduction to 30 % and LES to about 40 %, see Fig. 13b, of the initial circulation, whereas in case of a flat ground the circulation does not change significantly during this early time period. We observe that further away from the obstacle the circulation

[1] In a distance of $\Delta x^* = 1.05$ not enough data could be acquired after $t^* = 3$ to evaluate statistics.

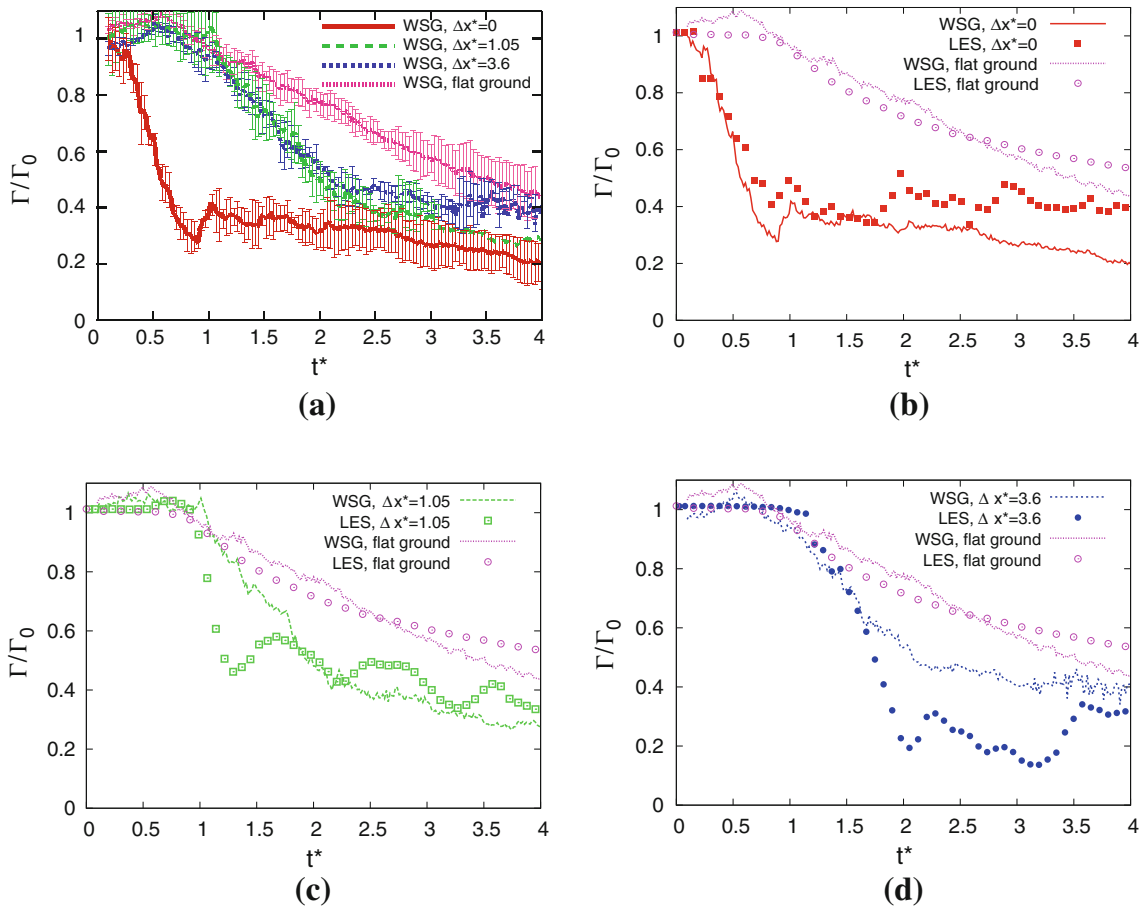


**Fig. 13** Vortex circulation maxima $\Gamma_{max}$ derived from PIV with standard deviations (**a**) and comparison with LES (**b**), (**c**), (**d**) at different distances from a square obstacle

is also reduced faster and stronger. Note that at a time of $t^* = 0.8$ above the obstacle the steep decrease of circulation stops abruptly and recovers to a slightly higher level. We observe this behavior in experiments as well as in LES. Particularly in the LES we also observe a recovery of circulation in slices apart from the obstacle. Qualitatively, experiments and LES agree well, see Fig. 13b–d. In particular for times smaller than $t^* = 1.8$ we observe also good quantitative agreement. However, the circulation is further reduced in experiments than in the LES for $t^* > 3$, in the case of a flat ground, and $t^* > 1.8$ above the obstacle. The higher circulation levels above the obstacle might be an explanation for the higher rebound characteristics, see Fig. 12. The reason for this behavior above the obstacle is not clear and may potentially also be related to an insufficient horizontal resolution of the secondary vortices in the LES. Additionally we suppose that the idealized conditions in the LES do not include all relevant sources of turbulence that influence the decay. In Fig. 13d we observe strong deviations of LES results from the experiments at $\Delta x^* = 3.6$ after a time $t^* = 1.8$. This can be explained by vortex bursting due to boundary effects, that have to be taken into account at this position, further reducing the circulation, compare Sect. 7.

The presented results are derived for low Reynolds number vortex flow. These low Reynolds number investigations need to be assessed at realistically high Reynolds numbers to determine how these results apply to aircraft and potential reduction of ICAO separations. The limitations of a high *Re* LES for boundary layer flow are addressed in [12]. Also it is impossible to achieve realistically high *Re* in towing tanks. Hence, flight experiments are mandatory to prove the stated effects in reality. However, it is known from flight measurements [5] that wake vortex trajectories, descent height, and rebound characteristics in ground proximity compare well with low *Re* simulations. Thus we believe that the strength of secondary vortices is similar and the effects presented here scale well.

## 6 Propagation of end effects

The helically looped secondary vortices generated by the obstacle, travel streamwise up and down along the primary

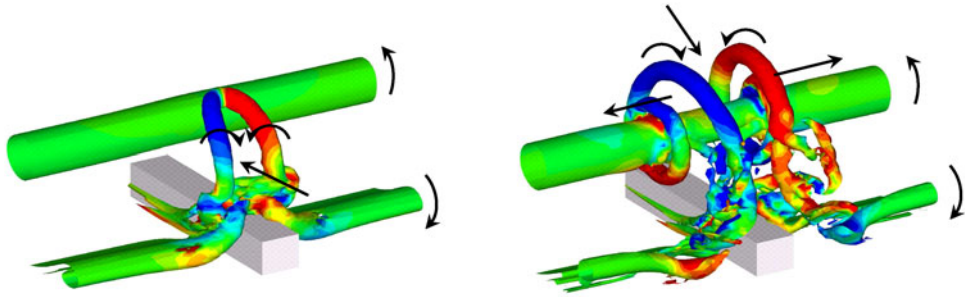

**Fig. 14** Omega-shaped SVS detaches from the obstacle in LES and induces a velocity towards the primary vortex (*left*); rolled-up SVS induces streamwise propagation velocity (*right*)

vortex and interact intensely with it, see Fig. 9. The vortex dynamics, detailed in Ref. [12], feature five characteristics.

1. *Early detachment of strong omega-shaped secondary vortices*

Above the obstacle secondary vortices detach earlier and are slightly stronger than the regular secondary vortices generated on a free surface.

2. *Omega-shaped secondary vortex approaches the primary vortex by self-induction*

The Ω-shaped secondary vortex is stretched in the flow field of the primary vortex and induces itself a velocity towards the primary vortex core, leading to a fast approach, see Fig. 14 (left). When approaching the primary vortex core the tip of the Ω-shaped secondary vortex aligns with the primary vortex. Since both vortices have vorticity of opposite sign the total circulation is reduced by the amount of the circulation of the secondary vortex. This effect is evident from the steep drop of circulation over the obstacle at $\Delta x^* = 0$ in Fig. 13a, b.

*3. After the secondary vortex has looped around the primary vortex it travels along the primary vortex again driven by self-induction*

The secondary vortex induces itself a radial velocity towards the primary vortex and an axial velocity resulting in a helical motion along the primary vortex, see Fig. 14 (right).

*4. Since the secondary vortex over the obstacle is connected to the vortices emerging from the flat boundary, the self-induced motion is continuously supplied with energy*

*5. Highly intense interaction of primary and secondary vortices leads to rapid wake vortex decay.*

The second and third characteristics are related to two kinds of so-called end effects transporting fluid axially up and down along the vortex [12]. First, the helix transports fluid in axial directions of the primary vortex. This leads to the accumulation of the tracer ink in the experiment visible in the snapshots, Fig. 10 (left). The second effect stems from a reduction of circulation at the obstacle, corresponding to a pressure increase inside the vortex core which propagates along the vortices [36]. Both effects are different in propagation speed and impact on circulation decay [12]. These effects can occasionally be observed at the wings of landing aircraft when trailing vortices marked by condensation droplets quickly disappear immediately after touch down [37, 38]. This indicates that the described physical mechanisms of vortex interaction could also explain the end effect of a vanishing vortex when the aircraft has landed [12]. The knowledge of the propagation speed of the disturbance and the related circulation decay is important for the optimal design of a WVAS where the decay of wake vortices, close to the touch down zone, or a suitable distance between adjacent obstacles, needs to be predicted.

Here we will investigate the first end effect that triggers the circulation decay more in detail, though the propagation speed is slower. In [12] it is pointed out that the passage of the helical disturbance correlates with a circulation reduction. In the experiments we observe that the onset of rapid decay at distances $\Delta x^* = 1.05$ and $\Delta x^* = 3.6$ does not agree with this statement, Fig. 13a. We believe that this can at least partly be explained by measurement uncertainties at early times. As we observe in the simulation, Fig. 10 (right), tracer is agglomerated at the head of the secondary vortex helix. In the experiments, Fig. 10 (left), we observe an ink package traveling up and down the vortex, which corresponds to the head of the invisible vortex spiral.

We compare the propagation speed of the helix in experiment and LES. In the experiments the disturbances travel either in towing direction or against it, see Fig. 10. From the video we estimate a speed of 0.5 or 0.4 m/s, respectively, which corresponds to 0.45 m/s if we subtract the speed coming from the wake. Hence we have a propagation speed normalized by the wake vortex descent speed of $U^*_{\mathrm{hel}} = 9.2$.

Figure 15 shows the propagation speed of the helix derived from the LES data. The red line depicts the speed of the helix depending on the distance to the obstacle. In the first phase the speed rises until it reaches an approximately constant level. Due to the interaction with the simulation domain boundary the propagation finally decelerates.

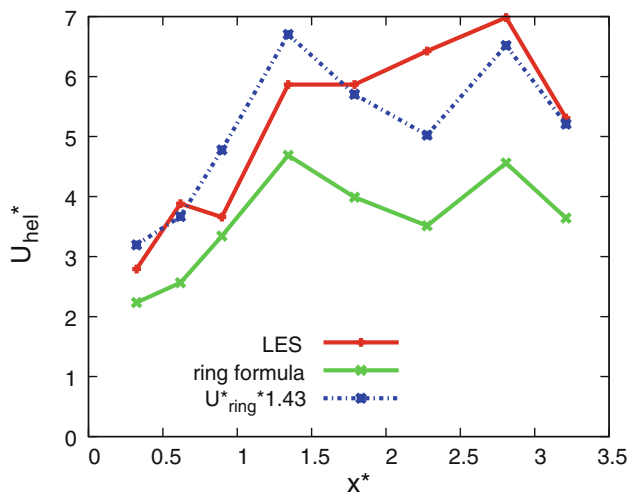


**Fig. 15** Propagation speed of helix from LES compared with theoretical speed of a vortex ring

We investigate the scalability of the propagation speed. Therefore, we approximate the spiral disturbance as a ring which is a good approximation at least in the first stage of its roll-up [12]. Vortex rings move with a self-induced velocity that depends on ring radius $R$, core radius $a$, and circulation $\Gamma$ of the ring vortex. If we neglect viscosity, the induced ring speed of a thin vortex ring $U_{\text{ring}}$ can be computed with the following formula [39]:

$$U_{\text{ring}} = \frac{\Gamma}{4\pi R}\left(\log\frac{8R}{a} - 0.25\right). \tag{12}$$

We evaluate the circulation $\Gamma^*_{\text{hel}}$ and the helix radius $R^*_{\text{hel}}$, see Table 2, of the secondary vortex helix at the helix front for different time steps. The helix core radius $a^*_{\text{hel}}$ is estimated from the visualizations, see Table 2. With these quantities we compute the propagation speed according to Eq. (12), see Fig. 15.

Apparently Eq. (12) underestimates the observed propagation speed. In particular, in the later stage the propagation speed of the conical and tapered-shaped helix deviates from the propagation speed, which we would expect from the vortex ring formula. On average the ratio $A = U^*_{\text{hel}}/U^*_{\text{ring}}$ equals 1.43. We take it as a correction factor for calculating $U^*_{\text{hel}} = A \cdot U^*_{\text{ring}}$, see Fig. 15.

The initial core radius of the primary vortex in the experiment is 0.0085 m. Assuming that the circulation, ring radius, and core radius of the secondary vortex scale with the corresponding circulation and the core radius of the primary vortex, Eq. (12) provides a propagation speed of 0.34 m/s again underestimating the observed value of 0.45 m/s. Hence, Eq. (12) supports scaling of the propagation speed between experiments and LES to first order and enables to estimate the propagation speed of the disturbance depending on initial circulation and primary vortex core radius. The experiments provide a scaling factor $A = U^*_{\text{hel}}/U^*_{\text{ring}}$ of 1.32. These results suggest that a fair approximation of the propagation speed of the helical disturbance may be achieved employing a correction factor of about 1.4.

**Table 2** Parameters of secondary vortex helix evaluated from LES

| $t^*$ | $x^*$ | $U^*_{\text{hel}}$ | $\Gamma^*_{\text{hel}}$ | $R^*_{\text{hel}}$ | $a^*_{\text{hel}}$ | $U^*_{\text{ring}}$ | $U^*_{\text{hel}}/U^*_{\text{ring}}$ |
|---|---|---|---|---|---|---|---|
| 0.30 | 0.32 | 2.8 | 0.12 | 0.082 | 0.02 | 2.2 | 1.27 |
| 0.38 | 0.62 | 3.9 | 0.16 | 0.104 | 0.02 | 2.6 | 1.5 |
| 0.46 | 0.90 | 3.7 | 0.23 | 0.123 | 0.02 | 3.3 | 1.12 |
| 0.53 | 1.34 | 5.9 | 0.24 | 0.081 | 0.02 | 4.7 | 1.26 |
| 0.61 | 1.79 | 5.9 | 0.21 | 0.087 | 0.02 | 4.0 | 1.48 |
| 0.68 | 2.28 | 6.4 | 0.18 | 0.079 | 0.02 | 3.5 | 1.83 |
| 0.76 | 2.81 | 7.0 | 0.20 | 0.064 | 0.02 | 4.6 | 1.52 |
| 0.84 | 3.21 | 5.3 | 0.19 | 0.080 | 0.02 | 3.6 | 1.47 |

## 7 Effects of several obstacles

Considering more than one obstacle leads to the question how the previously discussed disturbances interact. Assuming sufficiently large separations of the obstacles, we have no interaction of the omega-loops at the early stage of the flow, but during the propagation along the primary vortices. Note two main differences between simulation and experiment. While in our setting simulations with streamwise periodic boundary conditions cannot avoid the influence of neighboring obstacles, we have to put several obstacles in the experiments on purpose.

Second, in our simulations we assume fully rolled-up vortices approaching both obstacles at the same time. Consequently, we have a symmetric situation, where the collision of the propagating disturbances occurs exactly in the center between two obstacles. In the experiments the second obstacle will influence the wake vortex with an offset in time due to the towing speed, whereas in real approaches the flight speed is partly compensated by the aircraft descent. As a consequence, the point of collision of the disturbances is shifted axially. Hence, we have a symmetric situation in simulations and an asymmetric one in experiments and reality.

The collision of the propagating disturbances can be seen in the snapshots at $t^* \sim 0.8$ taken from the towing tank experiments with two obstacles, see Fig. 16 (left). As mentioned, we still use our above described simulations with periodic boundaries. For visualization in Fig. 16 (right) we just cut one half of the domain and connect it from the other side to the other half. We observe approaching disturbances, coming apparently from two obstacles and an accumulation of fluid, marked by a tracer, initialized in the vortex core, in both experiment and simulation. Eventually, the

disturbances collide and the vortex bursts. The good qualitative agreement between experiment and simulation provides confidence in the two methods and the interpretation that the tracer is actually transported and accumulated at the head of the propagating disturbances. Similar effects are discussed thoroughly in Ref. [32].

Figure 17 shows the development of the core radius for different configurations in the experiment (left) and the LES (right). We clearly see core radius maxima, caused by the disturbance passing the measuring plane in the experiment. First after the passage of the disturbance propagating in towing direction at $t^* = 1.5$ and then after the passage of the disturbance against towing direction at $t^* = 3$. After the passage of the second disturbance at $t^* \geq 3$ the core radius increases from $r_c^* = 0.07$ at $t^* = 0.5$ to $r_c^* = 0.25$ at $t^* = 3.3$. Once more the circulation reduces significantly, see Fig. 18. After the passage of the disturbances the core radius shrinks again. On the other hand, we see in simulations a growing core radius at the front of the helical vortex train, which is further increased again by a factor of four, where the disturbances collide. This is consistent with the bursting ink traces in the snapshots in Fig. 16. Maximum core radii occur where the disturbances collide, see Fig. 16.

## 8 Conclusion

We present a method to accelerate aircraft wake vortex decay in ground proximity using suitable obstacles at the ground. In the present work we investigate the influence of a block-shaped obstacle with a squared cross section on a pair of wake vortices generated above the obstacle. We perform experiments in a water towing tank, as well as wall-resolved large eddy simulations to analyze the flow field and quantify the decay. Wake vortex general behavior, decay, and rebound height are compared in the case of a flat ground as well as an obstacle at the ground.

In a water towing tank, a generic aircraft wing model is towed over flat ground as well as obstacles. A vortex core visualization using black ink is employed to get both a first qualitative overview and a global quantitative characterization. Velocity vector fields are recorded by stereo PIV for quantitative analysis. A vortex tracking evaluation is performed allowing the determination of the vortex core trajectories in selected cross planes, as well as vortex parameters like circulation strength and core radius. In order to create comparability with the experiments, a passive tracer, distributed in the vortex core, was used in LES. In the case of a flat ground we model the turbulent strut wake as the most important source of turbulence.

Both experiment and LES show that the well-known wake vortex flow in ground proximity is significantly disturbed by the obstacles. The disturbance first appears above the obstacle and then propagates axially along the wake vortices visualized by an accumulation of the tracer. This end effect phenomenon arises from propagating helical vortex structures that develop from the rolled-up secondary vortices at the obstacle. The quantitative analysis of the flow field, measured with time-resolved PIV, reveals that

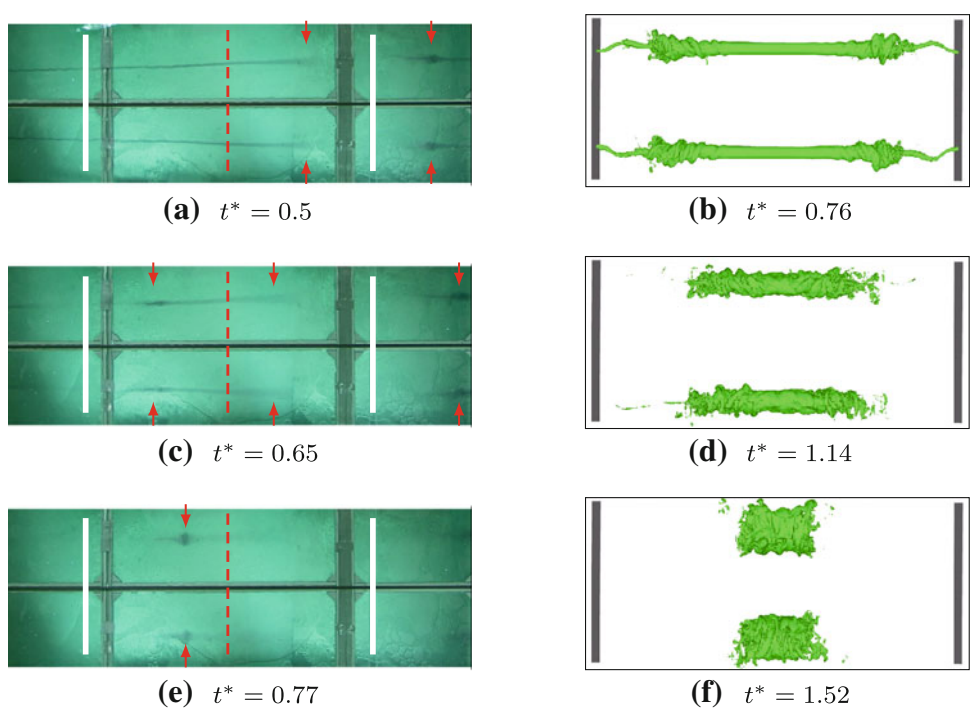


**Fig. 16** Effect of two obstacles. Vortex core visualization in towing tank with ink (**a**), (**c**) and (**e**), obstacles *left* and *right*, *dashed line* PIV measurement plane, distribution of passive tracer in LES (**b**), (**d**) and (**d**)

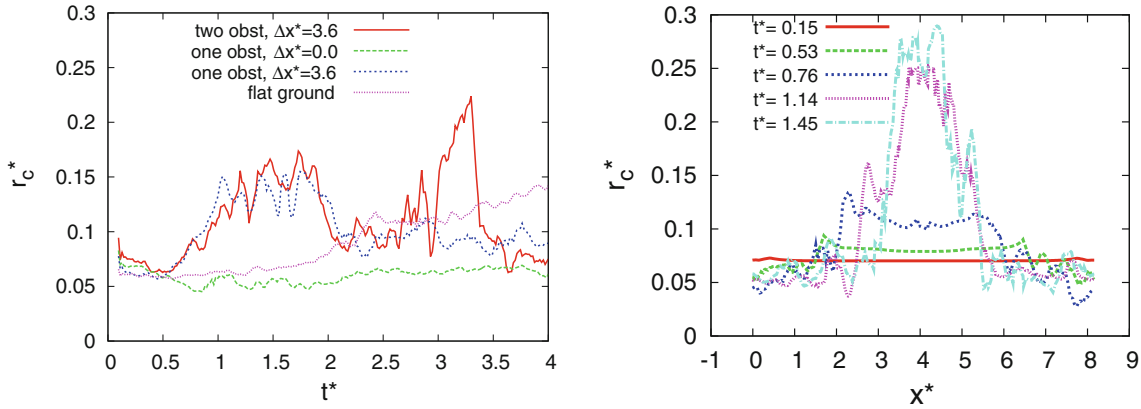


**Fig. 17** Vortex core radius along the vortex center line derived from PIV (*left*) for different distances from the obstacle and from LES (*right*) for different time steps

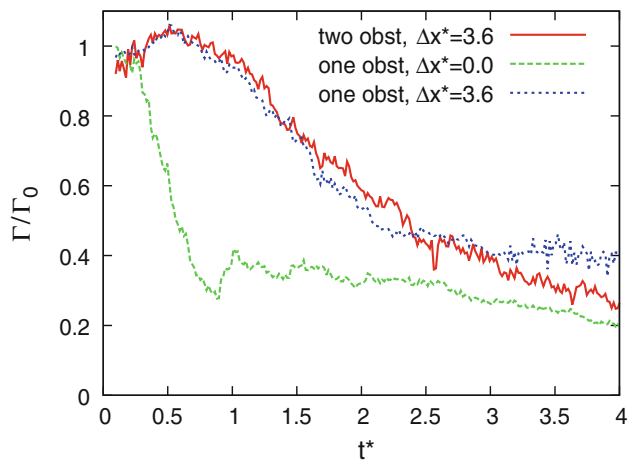


**Fig. 18** Vortex circulation maxima $\Gamma_{max}$ derived from PIV at different distances from one or two $0.2b_0 \times 0.2b_0$ square obstacles

the circulation is reduced significantly by obstacles in qualitative agreement with LES. At early times the decay process could be reproduced consistently, whereas at later times the circulation in the LES is too high with flat ground and directly above the obstacle, and too low at a larger distance, originating in a lack of turbulence and boundary effects, respectively. Also the vortex core trajectories depending on the distance to the obstacle first agree well, while for later times deviations are observed, depending on the distance to the obstacle. Reasons for the deviations in rebound height at the obstacle are the strong variability of the disturbed vortex in the experiments above the obstacle, a lack of turbulence in the LES, and possibly an insufficient resolution of secondary vortices. We believe that the observed vortex disturbance will also occur for realistic Reynolds numbers. The simulations indicate that flight safety could be improved and/or ICAO separations of aircraft might be reduced if the presented method for the enhancement of wake vortex decay would be applied and an appropriate wake vortex advisory system would be installed.

We investigate the propagation speed of the disturbance in the experiment as well as in the simulations and propose a propagation speed formula based on a thin vortex ring. The scalability of this simple model appears reasonable. Future flight experiments will have to confirm this approach. Colliding disturbances generated by two obstacles lead to vortex bursting and additionally support the decay process. In summary, the introduction of obstacles at the ground supports the selective generation of secondary vortices and smart utilization of vortex properties to generate fast approaching and rapid spreading of disturbances along the primary vortex leading to premature vortex decay in ground proximity. The installation of suitable obstacles in the area in front of the runway ends may improve safety by reducing the number of wake encounters and increase the efficiency of wake vortex advisory systems. A respective patent has been filed under number DE 10 2011 010 147. In the meanwhile, flight experiments have been conducted at Oberpfaffenhofen airport (Germany) that confirm that obstacles actually accelerate wake vortex decay in ground proximity.

**Acknowledgments** The simulations have been performed using supercomputers at Leibniz-Rechenzentrum (LRZ). We would like to thank Prof. M. Manhart for providing the original version of the LES code MGLET. The work was funded by DLR project Wetter & Fliegen.

## References

1. Gerz, T., Holzäpfel, F., Bryant, W., Köpp, F., Ferch, M., Tafferner, A., Winckelmans, G.: Research towards a wake-vortex advisory system for optimal aircraft spacing. C. R. Phys. **6**(4–5), 501–523 (2005)
2. Gerz, T., Holzäpfel, F., Darracq, D.: Commercial aircraft wake vortices. Prog. Aerosp. Sci. **38**(3), 181–208 (2002)

3. Spalart, P.: Airplane trailing vortices. Annu. Rev. Fluid Mech. **30**(1), 107–138 (1998)
4. Critchley, J., Foot, P.: UK CAA wake vortex database: analysis of incidents reported between 1982 and 1990. Civil Aviation Authority, CAA Paper, vol. 91 (1991)
5. Holzäpfel, F., Steen, M.: Aircraft wake-vortex evolution in ground proximity: analysis and parameterization. AIAA J. **45**, 218–227 (2007)
6. Robins, R., Delisi, D.: Potential hazard of aircraft wake vortices in ground effect with crosswind. J. Aircr. **2**, 201–206 (1993)
7. Türk, L., Coors, D., Jacob, D.: Behavior of wake vortices near the ground over a large range of reynolds numbers. Aerosp. Sci. Technol. **3**(2), 71–81 (1999)
8. Harvey, J., Perry, F.: Flowfield produced by trailing vortices in the vicinity of the ground. AIAA J. **9**(8), 1659–1660 (1971)
9. Dufresne, L., Baumann, R., Gerz, T., Winckelmans, G., Moet, H., Capart, R.: Large eddy simulation of wake vortex flows at very high reynolds numbers: a comparison of different methodologies. Technical Report, AWIATOR, D1.14-16 (2005)
10. Proctor, F.H., Hamilton, D.W., Han, J.: Wake vortex transport and decay in ground effect: Vortex linking with the ground. In: AIAA, 2000-0757, 38th Aerospace Sciences Meeting & Exhibit, Reno (2000)
11. Spalart, P., Strelets, M., Travin, A., Shur, M.: Modelling the interaction of a vortex pair with the ground. Fluid Dyn. **36**(6), 899–908 (2001)
12. Stephan, A., Holzäpfel, F., Misaka, T.: (2013) Aircraft wake vortex decay in ground proximity—physical mechanisms and artificial enhancement. J. Aircr . http://arc.aiaa.org/doi/abs/10.2514/1.J051609. Accessed 19 June 2013
13. Coustols, E., Stumpf, E., Jaquin, L., Moens, F., Vollmers, H., Gerz, T.: Minimized wake: a collaborative research programme on aircraft wake vortices. AIAA Paper 2003-0938 (2003)
14. Stumpf, E.: Study of four-vortex aircraft wakes and layout of corresponding aircraft configurations. J. Aircr. 42, 722–730 (2005)
15. Breitsamter, C.: Wake vortex characteristics of transport aircraft. Prog. Aerosp. Sci. **47**, 89–134 (2011)
16. Duponcheel, M., Lonfils, T., Bricteux, L., Winckelmans, G.: Simulations of three-dimensional wake vortices in ground effest using a fourth-order incompressible code. In: 7th National Congress on Theoretical and Applied Mechanics, Mons (2006)
17. Georges, L., Geuzaine, P., Duponchel, M., Bricteux, L., Lonfils, T., Winckelmans, G., Giovannini, A.: Technical report 3.1.1-3, les of two-vortex system in ground effect with and without wind. Technical Report, Université catholique de Louvain (UCL), Institut de Mécanique des Fluides de Toulouse (IMFT) (2005)
18. Delisi, D.P.: Laboratory measurements of the effect of ambient turbulence on trailing vortex evolution. In: 44th AIAA Aerospace Sciences Meeting and Exhibits, San Reno (2006)
19. Cottin, C., Desenfans, O.G.D., Winckelmans, G.: Towing-tank visualization of two-vortex systems in ground effect. Technical Report, FAR-Wake, Université Catholique de Louvain (UCL) (2007)
20. Konrath, R., Carmer, C., Schrauf, G., Schmidt, K., Winckelmans, G., Cottin, C., Desenfans, O.G.D., Cocle, R.: Dynamics and decay of spatially-evolving two- and four-vortex wakes near the ground. Technical Report, FAR-Wake project deliverable D 3.1.2 (2008)
21. Hah, C., Lakshminarayana, B.: Measurement and prediction of mean velocity and turbulence structure in the near wake of an airfoil. J. Fluid Mech. **115**, 251–282 (1982)
22. Zhang, Q., Lee, S.W., Ligrani, P.M.: Effects of surface roughness and freestream turbulence on the wake turbulence structure of a symmetric airfoil. Phys. Fluids **16**(6), 2044–2053 (2004)
23. Manhart, M.: A zonal grid algorithm for dns of turbulent boundary layer. Comput. Fluids **33**(3), 435–461 (2004)
24. Meneveau, C., Lund, T.S., Cabot, W.H.: A lagrangian dynamic subgrid-scale model of turbulence. J. Fluid Mech. **319**, 353–385 (1996)
25. Holzäpfel, F.: Adjustment of subgrid-scale parametrizations to strong streamline curvature. AIAA J. **42**(7), 1369–1377 (2004)
26. Shen, S., Ding, F., Han, J., Proctor, F.H.: Numerical modeling studies of wake vortices: real case simulations. In: 37th AIAA Aerospace Sciences Meeting and Exhibit. Reno, Nevada, USA (1999)
27. Hokpunna, A., Manhart, M.: Compact fourth-order finite volume method for numarical solutions of Navier–Stokes equations on staggered grids. J. Comput. Phys. **229**(20), 7545–7570 (2010)
28. Misaka, T., Holzäpfel, F., Gerz, T.: Wake evolution of wing-body configuration from roll-up to vortex decay. In: 50th AIAA Aerospace Sciences Meeting including the New Horizons Forum and Aerospace Exposition, Nashville, Tennessee, USA., 2012-0428, pp. 1–15 (2012)
29. Béchara, W., Bailly, C., Lafon, P.: Stochastic approach to noise modeling for free turbulent flows. AIAA J. **32**(3), 455–463 (1994)
30. de Bruin, A., Winckelmans, G.: Cross-flow kinetic energy and core size growth of analytically defined wake vortex pairs. Technical Report, NLR-CR-2005-412, NLR (2005)
31. Holzäpfel, F., Hofbauer, T., Darracq, D., Moet, H., Garnier, F., Ferreira Gago, C.: Analysis of wake vortex decay mechanisms in the atmosphere. Aerosp. Sci. Technol. **7**, 263–275 (2003)
32. Misaka, T., Holzäpfel, F., Hennemann, I., Gerz, T., Manhart, M., Schwertfirm, F.: Vortex bursting and tracer transport of a counter-rotating vortex pair. Phys. Fluids **24**, 025,104-1–025,104-21 (2012)
33. Holzäpfel, F.: Probabilistic two-phase wake vortex decay and transport model. J. Aircr. **40**(2), 323–331 (2003)
34. Konrath, R., Pallek, D., Mattner, H., v. Cramer C.: Analysis of flow field measurements obtained in a large tow tank regarding the decay of wake vortices in the far-field for two- and four-vortex systems. In: AIAA-Paper 2009-342, 47th AIAA Aerospace Science Meeting, Orlando (Florida) (2009)
35. Holzäpfel, F., Gerz, T., Baumann, R.: The turbulent decay of trailing vortex pairs in stably stratified environments. Aerosp. Sci. Technol. **5**(2), 95–108 (2001)
36. Moet, H., Laporte, F., Chevalier, G., Poinsot, T.: Wave propagation in vortices and vortex bursting. Phys. Fluids **17**, 054,109 (2005)
37. http://www.youtube.com/watch?v=KqU70RORXtA
38. http://www.youtube.com/watch?v=oHGqxM1-rAI
39. Lamb, H.: Hydrodynamics. Cambridge University Press, London (1957)